LES-RANS study of serrated nozzle jet aeroacoustics for an installed Ultra-High-Bypass-Ratio aeroengine

Zhong-Nan Wang,* James C. Tyacke,† Paul G. Tucker‡

Department of Engineering, University of Cambridge, Cambridge, CB2 1PZ, UK

Jet noise is amplified at low frequencies when the jet is installed under a wing. Serrations are designed at the nozzle exit to mitigate installation noise generation. In this paper, LES-RANS is performed to investigate the serration effects on installed jet flows and acoustics in an industrially relevant configuration, an Ultra-High-Bypass Ratio (UHBR) aeroengine mounted under a three-dimensional wing. The results show that the serrations are able to weaken jet and wing interactions and consequently reduce far-field installation noise. The noise reduction mechanisms have been sought through the quadrupole sources in the jet plume and evanescent pressure wave scattering at the wing trailing edge.

Nomenclature

c	Sound speed, m/s
Cp	Surface pressure fluctuation coefficient, $p'/(\rho_a u_a^2)$
D	Bypass nozzle diameter, m
d	wall distance, m
f	Frequency, Hz
m	Azimuthal mode number
$\dot{m}$	Mass flow rate, kg/s
M_a	Mach number, $\lvert u\rvert/c_a$
p	Pressure, Pa
St	Strouhal number (nondimensional frequency), fD/U
T	Temperature, K

*Lecturer (currently), College of Engineering and Physical Sciences, University of Birmingham, and member AIAA.
†Lecturer (currently), Department of Mechanical and Aerospace Engineering, Brunel University London, and member AIAA.
‡Rank Professor of Engineering, Department of Engineering, University of Cambridge, and Associate Fellow AIAA.

Ti Turbulent intensity, K

t Time, s

u Velocity, m/s

U Jet velocity of bypass nozzle, m/s

$\mathbf{x}$ Location vector, (x, y, z) in the catesian coordinates or (x, r, θ) in the cylindrical coordinates, m

ρ Density, m/s

ϕ Polar angle, $^\circ$

Ω Vorticity, $1/s$

Subscript

a Ambient

rms Root mean square

$i, j, k,$ Coordinate indices

0 Staganation

I. Introduction

Noise is ranked at the top of public perception list of aviation impact and it becomes a key factor for certification of newly developed aircrafts. Aeroengine exhaust jet flows contribute significantly to aircraft noise and the sound power level scales with jet velocity to the eighth power.[1] When the jet is placed underneath a solid surface, the far-field noise is further amplified at low-frequencies by scattering hydrodynamic instability waves at the surface edge.[2–4] This senario occurs when a jet engine is installed under an aircraft wing. It was found that the installation noise exhibits a dipole-like directivity pattern in the far-field and scales with the jet velocity to the $5 - 6^{th}$ power.[5,6] The amplification increases when the jet is installed closer to the surface edge. For future generation engines, Ultra-High-Bypass-Ratio (UHBR) is employed to increase propulsion efficiency. Thus, the engine has to be installed at a smaller distance to the aircraft wings due to the constraint imposed by safe ground clearance. Hence installation noise becomes more severe. This makes the engine and airframe integration even more challenging.

The latest ACARE (Advisory Council for Aeronautics Research in Europe) report[7] sets a vision to reduce aircraft noise certification levels by 97% (i.e. 15 dB) by 2050. This will not be possible without substantial research into effective noise reduction strategies. Among the noise reduction strategies, serrations built on exhaust nozzles, also known as chevrons, have been confirmed to be effective and practical to reduce jet noise. It is found that serrations introduce streamwise vorticy, increasing near-nozzle flow mixing and shifting acoustic energy from low to high frequencies.[8] Serrations are capable of reducing the low-frequency

noise particularly at downstream polar angles. Much of the research on nozzle serrations is currently focused on isolated jets,[9] but the effect of serrations on installed jet flow and acoustics has received less attention. As future UHBR engines intensify installation noise, it becomes necessary and urgent to investigate whether and how serrations can be used to effectively reduce installation noise. Mengle has made some early attempts to reduce installation noise by designing azimuthally varying chevrons.[10] He measured the farfield noise and found the azimuthally varying chevrons capable of further reducing far field noise compared to azimtually uniform chevrons . However, how this noise reduction has been achieved cannot possibly be understood using acoustic data only. The detailed flow field is needed to understand the mechanisms and guide effective noise reduction design in the future.

While measuring high-speed jet flows with wing installation is extremely challenging, large eddy simulation (LES, the cost $\propto Re^{2.4}$) provides a feasible solution to obtaining high-fidelity flow field data when compared with direct numerical simulation (DNS, the cost $\propto Re^{3}$).[11,12] LES offers opportunities to look into sound sources in great detail and investigate possible noise reduction methods. LES is promising for high Reynolds number flows but it remains expensive to resolve coherent turbulent structures near the wall.[13] Reynolds Averaged Navier-Stokes (RANS) equations are solved for flow near the solid boundary and hybridised with LES for the outer layer to further reduce the cost to the level $\propto Re^{0.6}$.[14] Hybrid LES-RANS has been successfully developed to simulate installed jets from canonical[15] to industrial levels.[16,17] In the above, turbulence statistics and dynamics are captured in the jet plume by LES from first principles. The far-field sound was accurately predicted by performing Ffowcs William-Hawkings (FW-H) integration using near-field LES flow data. The methods are also sucessfully used to predict noise reduction for isolated chevron jets from single-stream nozzles[18] to dual-stream nozzles.[19]

In this paper, hybrid LES-RANS is performed on an installed UHBR engine to investigate serration effects on jet turbulence and its associated acoustics. Following a brief description of the computational methods and cases, the near-field flow and far-field acoustics are directly compared between the round and serrated nozzle jets to evaluate serration effects. Further analyses are then performed on near-field flows to find possible mechanisms via which the noise reduction has been achieved by serrations.

II. Computational Cases and Settings

The cases focused on here are a baseline round nozzle and a serrated nozzle placed under a finite-span three-dimensional wing. Figure 1 shows the configuration for the installed serrated nozzle jet. The wing trailing edge sits at $2D$ from the bypass nozzle exit plane and $0.5D$ vertically from the nozzle centre line. The number of serrations ($N_{serration}$) is 16. These are integrated on the periphery of the round nozzle exit. The nozzles comprise core and bypass ducts. They operate at different temperature and pressure ratios with

a bypass ratio of 15.4, listed in Table 1. The jet and wing are immersed in a forward flight stream at a Mach number of 0.26. The results of isolated round and serrated nozzle jets[19] are also used here when installation effects are discussed.

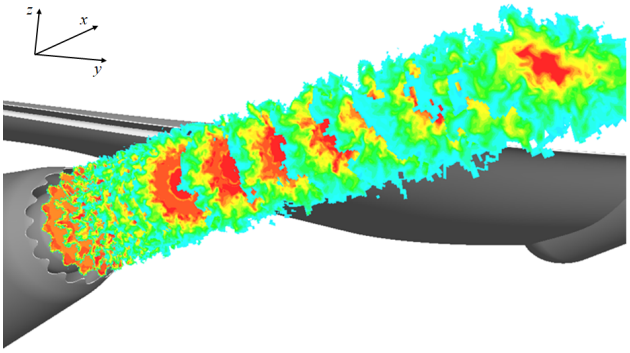

Figure 1. Installation configuration of serrated nozzle jet with axial velocity countours at axial planes

Table 1. Jets operating conditions

	p_0/p_a	T_0/T_a	M_a	$\dot{m}(kg/s)$
Bypass	1.342	1.128	0.67	6.373
Core	1.222	2.652	0.86	0.414

The computational domain extends $60D$ axially downstream of the jet exit and $30D$ radially from jet centre line. The LES region is restricted to the jet plume and near-field region, namely $r \leq 6D$ and $-5D \leq x \leq 30D$, and then blended into sponge zones to prevent boundary reflections. Figure 2 shows the modular structured-unstructured mesh generated to accommodate this complex installation geometry. The jet plume is meshed by hexahedral elements interfacing with tetrahedral elements in the acoustics region. The mesh is made to align with jet shear layer development. More details about the mesh, especially for the installed round jet, can be found in our previous publication.[16] Shear layers from serrated nozzles vary periodically in the azimuthal direction and introduce finer turbulence scales. The mesh is refined azimuthally near the nozzle in order to resolve the serrations and their induced flow structures. The mesh is gradually coarsened azimuthally downstream and matches the round jet mesh resolution where the azimuthal variation of shear layer disappears. The mesh statistics of element number N in each cell type and total number of grid nodes N_{node}, cells N_{cell} and edges N_{edge} are shown in Table 2 for the two installed jets.

Table 2. Mesh statistics for installed round and serrated nozzle jets ($N \times 10^6$)

	N_{node}	$N_{Hex.}$	$N_{Tex.}$	$N_{Pyr.}$	$N_{Pri.}$	N_{cell}	N_{edge}
Installed round	62.4	44.4	78.4	1.24	7.8	131.8	224.1
Installed serrated	70.0	50.2	88.8	1.5	7.7	148.4	274.2

The solver used here is developed using unstructured edge-based finite-volume methods for compressible

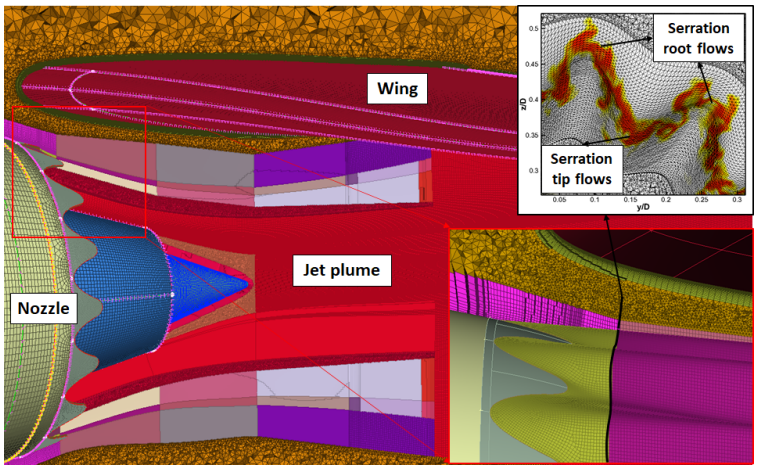

Figure 2. Modular structured-unstructured meshes for the installed serration jet

flows. A second-order kinetic energy preserving (KEP) method[20] is used in space to stablise the simulation without any numerical dissipation. Previous studies show the KEP scheme is insensitive to cell types compared to upwind schemes.[21] This enables the simulation to be performed on mixed types of elements. The second-order KEP scheme is combined with fourth-order Laplacian smoothing and grid stretching towards boundaries to prevent numerical reflections. Second-order backward differencing is used in time with dual-time stepping. The physical time step used in the simulation is $0.002D/U$ with data recorded every 10 time steps on FW-H surfaces and every 50 time steps in the jet plume. The pseudo time stepping is achieved using five-step Runge-Kutta methods. To alleviate demanding grid requirements near walls, a hybrid RANS-LES model is developed to solve the Spalart-Allmaras RANS model[22] for the inner wall boundary layer. The thickness of RANS layers varies over different parts of solid surfaces: Full boundary layer is covered by RANS on the external nacelle; A thinner RANS kayer is used until $y^+ = 200$ over the wing and flap underside to solve the substantial turbulence induced by jet and wing interactions, while a RANS layer with the thickness of $y^+ = 1000$ is applied on the interior of nozzle surfaces to model the majority of boundary layer flow. Outside of the RANS layer where larger scales dominate, LES is used with a mixed nonlinear subgrid-stress (SGS) model. The mixed nonlinear model comprises the Smagorinsky SGS model[23] as linear term to model dissipation and the alpha model[24] as nonlinear terms to model anisotropy. More details of the hybrid turbulence modelling can be found in the previous publication.[16] Acoustics prediction is achieved by integrating over a permeable FW-H surface. The FW-H surface is placed outside active hydrodynamic regions with the criteria: the wall distance $d_{wall}/D > 0.25$, the turbulence intensity $Ti < 0.25\%$ and the vorticity $|\Omega|D/U < 0.05$. A convective formulation of the FW-H equation[25] is used to include the flight stream effects on sound propagation. The methods presented here have been successfully used for a number of jet flow and noise prediction.[15,16,18,19]

III. Results

A. Near-field flow

The instantaneous flow from the installed serrated nozzle are featured in Fig. 1. High-speed bypass nozzle flow is ejected radially at serration roots and pushed inwards at serration tips. This introduces a pair of streamwise vortices for each serration. As a result of streamwise vortices, the lobbed shear layer is formed immediately downstream of the serrations. The periodic azimuthal variation is restricted near the nozzle and decays rapidly in the downstream. The jet-wing interactions take place further downstream and have a significant impact on the upper side of the jet plume.

The mean axial velocity and turbulent kinetic energy (TKE) of the serrated nozzle jet are directly compared with that of the round nozzle jet at four axial planes in Fig. 3. Near the nozzle ($x/D = 0.25$), the thin shear layers from both jets are not much affected by the wing and the periodic azimuthal variation in the serrated nozzle jet is significant. In the middle of the wing chord length ($x/D = 1$), the shear layer spreads out and the wing effects become apparent. The TKE in the upper shear layer is dissipated due to flow acceleration near the wing. The serrated nozzle thickens the jet shear layer as streamwise vortices enhance the entrainment of ambient fluid into the jet plume. At $x/D = 3$, immediately downstream of the wing tailing edge (TE), the azimuthal variation of the serrated nozzle jet is diminished as the streamwise vortices dissipate. The wing downwash distorts the jet plume and has a significant influence on the upper shear layer. An increased TKE level is observed in the upper shear layer as a result of jet and wing interactions. Compared to the round nozzle jet, serrations are able to mitigate this interaction and yields a lower level of TKE increase. At a further downstream station $x/D = 6$, the serrated nozzle jet becomes similar to the round nozzle jet and both of them exhibit an oval shape jet plume as impacted by wing downwash.

Figure 4 provides the development of shear layer under the wing at the planes that cut through nozzle centre line. The jet plume is deflected by the wing and extra TKE is produced just downstream of the wing (from $x/D = 2$ to 6) due to the interaction. Compared to the round nozzle jet, shear layers from the serration tip, shown in Fig. 4(c) and 4(d), and the serration root, shown in Fig. 4(e) and 4(f), exhibit different trajectories near the nozzle. The radial velocity variation between the root and tip shear layers generates streamwise vortices increasing mixing inside the shear layers. The TKE is first produced near the nozzle and then quickly dissipates downstream due to enhanced mixing. When the jet reaches the wing TE, the turbulence level is much less than that of the round jet. This results in a weaker interaction between the jet and wing. The reduced interaction is also evident from the surface pressure fluctuations on the wing in Fig. 5. Hence, the TKE production caused by the jet and wing interaction is decreased by the nozzle serrations and then has an impact on the sound sources that will be discussed later in the section C. The surface Cp_{rms} peak in Fig. 5(b) has separated into smaller lobes with the serrations. This indicates the

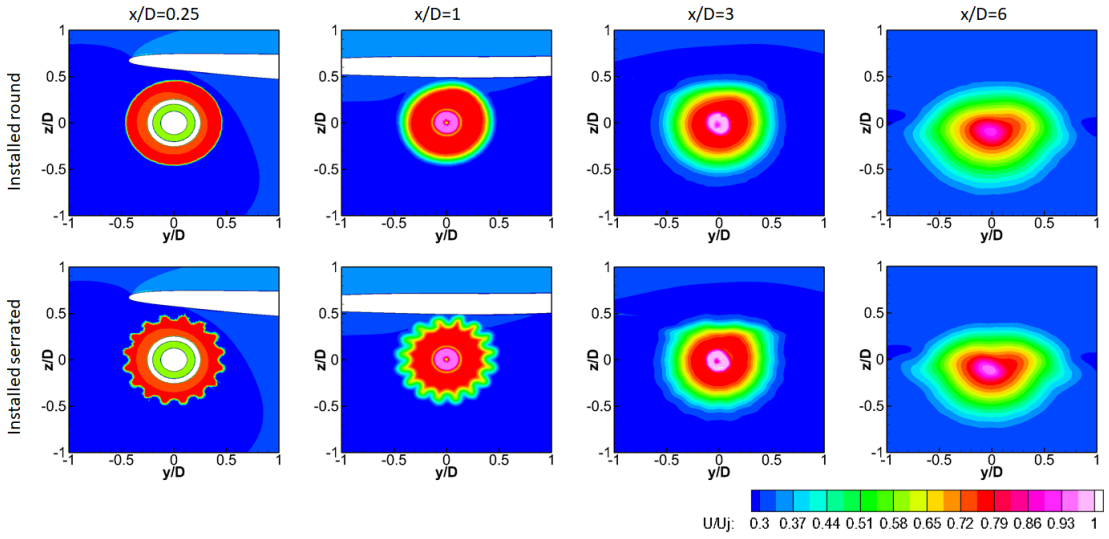

(a) Axial velocity

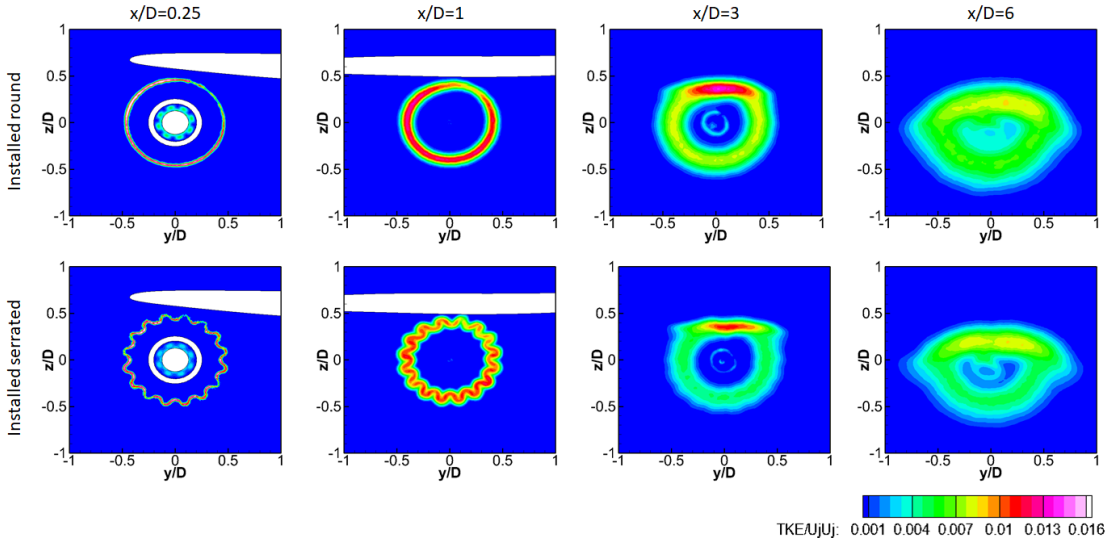

(b) Turbulent kinetic energy

Figure 3. Time-mean axial velocity and turbulent kinetic energy at axial planes for installed round and serrated nozzle jets

serrations have potential influence on the boundary layer development on the wing surface and the pressure wave scattering at the wing TE.

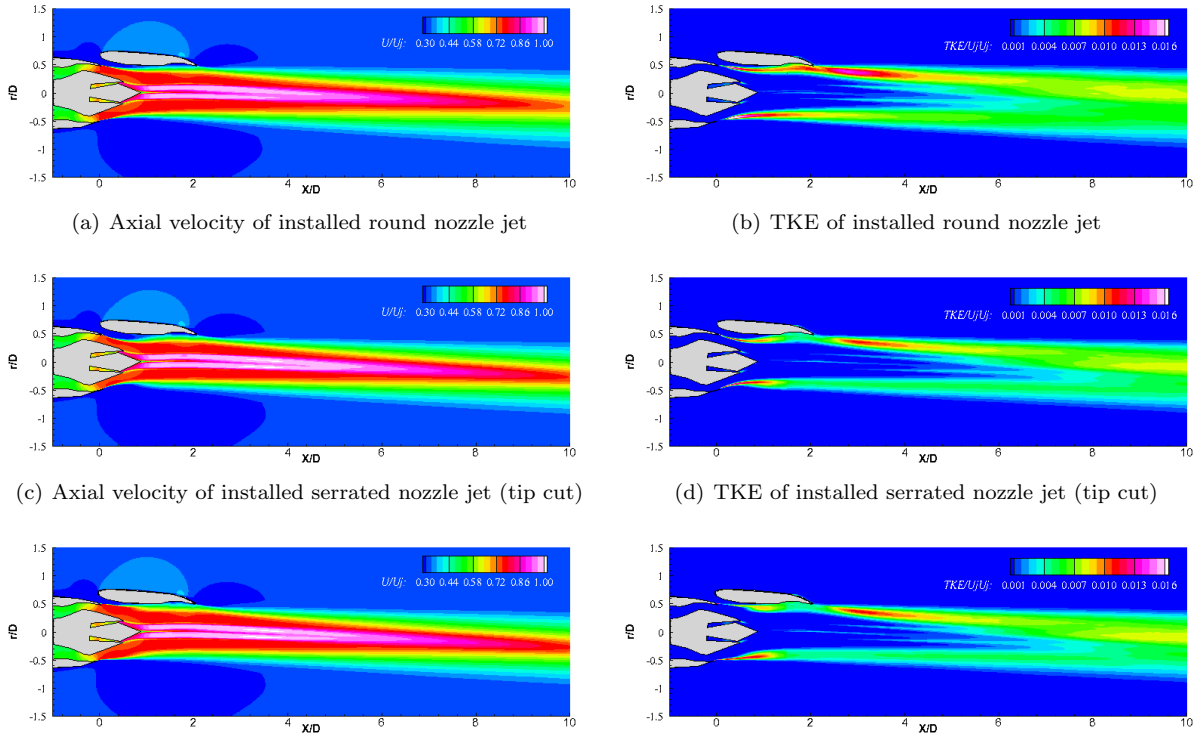

(a) Axial velocity of installed round nozzle jet

(b) TKE of installed round nozzle jet

(c) Axial velocity of installed serrated nozzle jet (tip cut)

(d) TKE of installed serrated nozzle jet (tip cut)

(e) Axial velocity of installed serrated nozzle jet (root cut)

(f) TKE of installed serrated nozzle jet (root cut)

Figure 4. Time-mean axial velocity and turbulent kinetic energy (TKE) at the $arctan(y/z) = 0$ plane for round nozzle jet and at the $arctan(y/z) = 0$ (serration tip cut) and the $arctan(y/z) = \pi/N_{serration}$ (serration root cut) plane for serrated nozzle jet

B. Far-field acoustics

Figure 6 shows the near-field flow structures and the acoustic waves emitted from these structures for the installed jet. Compared to the round nozzle jet, serrations are able to break up large-scale azimuthal coherent structures near the nozzle and generates small-scale structures, although the different azimuthal grid resolution near the serrated and round nozzles may have a potential limit on this comparison. The breakup of azimuthal coherence structures could physically be achieved by introducing extra shear from azimuthal variations of radial fluid movement (streamwise vortices). The resultant small-scale turbulence dissipates rapidly downstream as seen in Fig. 4. This supports the hypothesis proposed by Zaman et al.[9] that the early breakup of azimuthal coherence near the nozzle has a 'calming effect', reducing overall turbulence and correlates with the noise reduction. There are three groups of visible acoustic waves emitted from the near field: one is the mixing noise generated by the jet shear layers and the other two are generated at the leading and trailing edge (LE&TE) of the wing due to the jet and wing interactions. The TE scattering noise is considered more important and referred to as installation noise, because the TE lies in the active

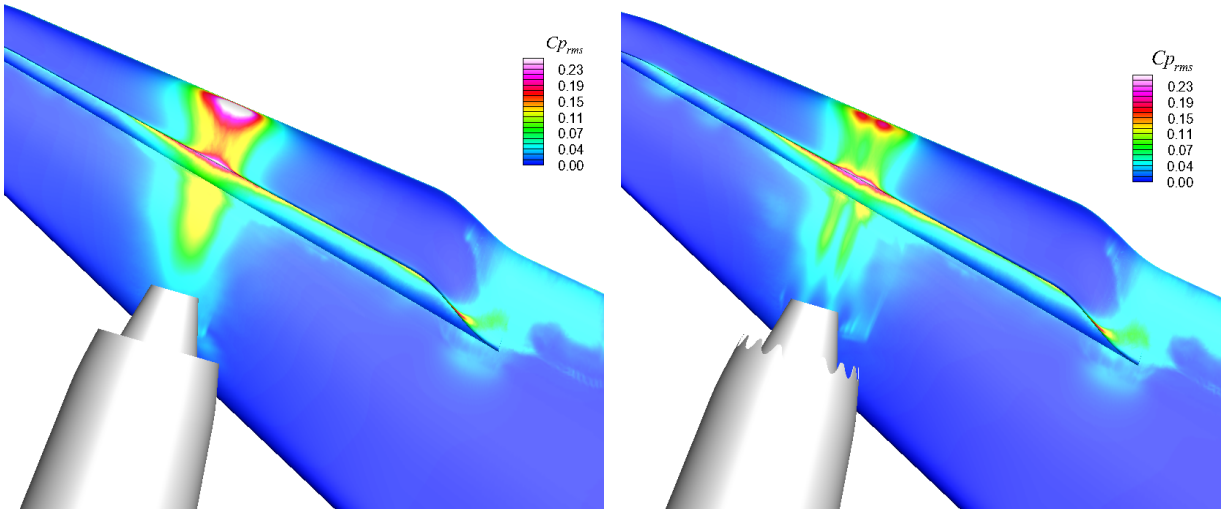

(a) Wing with the installed round nozzle (b) Wing with the installed serrated nozzle

Figure 5. The root mean square of surface pressure fluctuation Cp_{rms} on the underneath of the wing

hydrodynamic region. The waves emitted from the TE also have a longer wavelength than those of the LE. The TE scattering will be further discussed in the section C.2.

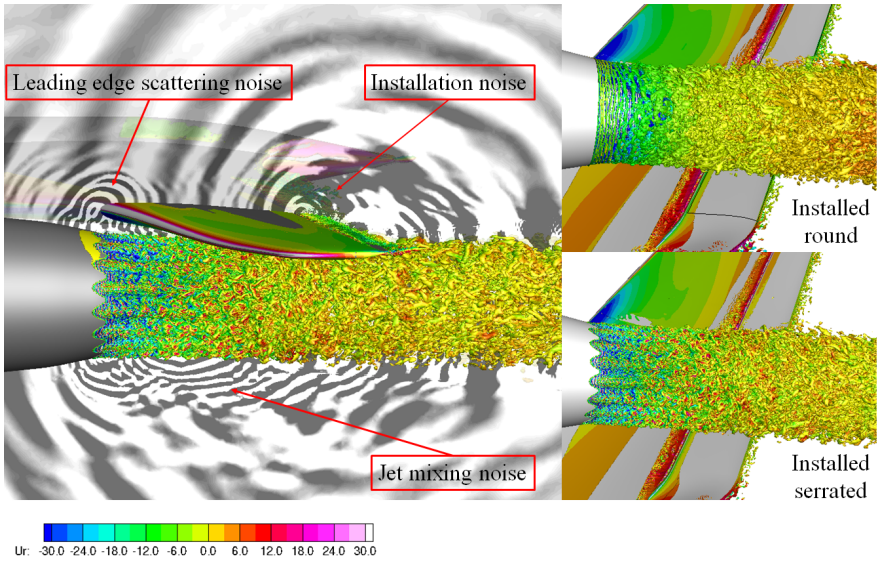

Figure 6. Iso-surfaces of Q-criterion coloured by radial velocities with the background contours of $\partial p/\partial t$

Far-field noise spectra are predicted using FW-H methods based on the near-field LES flow data and they are compared with experimental measurements in Fig. 7. The comparison is made at the flyover azimuthal position which is directly under the wing. The predictions are provided at four representative polar angles ($\phi = 30°, 70°, 90°$ and $110°$) where measurements are available. The polar angle at the fly-over location, right under the wing, is defined as $\phi = arctan(\frac{-z}{x})$, which is the angle between the observer location vector and positive x axis. In general, the prediction shows a satisfactory agreement with the far-field acoustic

measurements. The numerical cut-off of predicted spectra is around $St = 2$. The noise prediction of isolated round jet agrees better with the experimental measurements than that of the installed jet. This is because the data for the installed jet experiment, which was conducted in a different facility,[26] may be subject to some internal noise from the supply pipe. This could be the reason for the under-prediction of low and high frequency end at the polar angle $\phi = 30°$ and the peak at higher polar angles, such as $\phi = 110°$ for the installed jet. Compared to the isolated jet, a noise increase is observed for the installed jet in the middle range of the presented spectra. This installation noise increases with the polar angle and becomes more pronounced in the upstream polar angles. The level and polar variation of this noise amplification are consistent with that found in the historic experiments.[5] Comparing the installed round and serrated nozzle jets, a noise reduction can be seen over all polar angles for installed serrated nozzle jet and the increase of noise reduction towards high polar angles suggests the effectiveness of using serrations to suppress installation noise. The noise is reduced by around 5dB at the peak frequency where the installation noise is significant. However, the mesh resolution limits high-frequency noise prediction hence the potential noise penalties introduced by serrations cannot be evaluated by the current simulation. It is fair to judge that the overall noise benefits of serrations will be smaller than what is shown in the presented spectra range.

As experiments have not been preformed on the presented serrated nozzle jet, the experimental data from a similar installed jet configuration is used here as a reference to indirectly verify the serrated nozzle simulation. This reference installed serration jet operates at similar core and bypass velocities but with a shorter distance from jet exit to wing TE. The serrations in the experiments are also shorter with less aggressive penetration angles than the ones in the simulation. The noise reduction is defined as the difference of far-field noise spectra between the installed baseline round nozzle and serrated nozzle jets. It is normalised by the local maximum value in order to make qualitative comparisons between the two configurations, shown in Fig. 8. The normalised serration noise reductions for the two installation configurations are similar in shape. The optimal noise reduction ranges from $St = 0.5$ to 1 with the peak moving slightly to high frequencies at high polar angles. This indicates that the current simulation has captured the characteristics of installed jet noise reduction by serrations, indirectly ensuring the simulation quality. Although the serrated nozzle jet prediction cannot be directly validated, the prediction method has been validated here on the round nozzle jets and also on our previous serrated nozzle jet.[18]

C. Sound sources

The noise generation of installed jets can be broken down into two categories:[3] quadrupole sources for jet mixing noise and TE scattering for installation noise. As a noise reduction has been seen for the installed serrated nozzle jet, the noise reduction mechanisms are sought through these two types of sources.

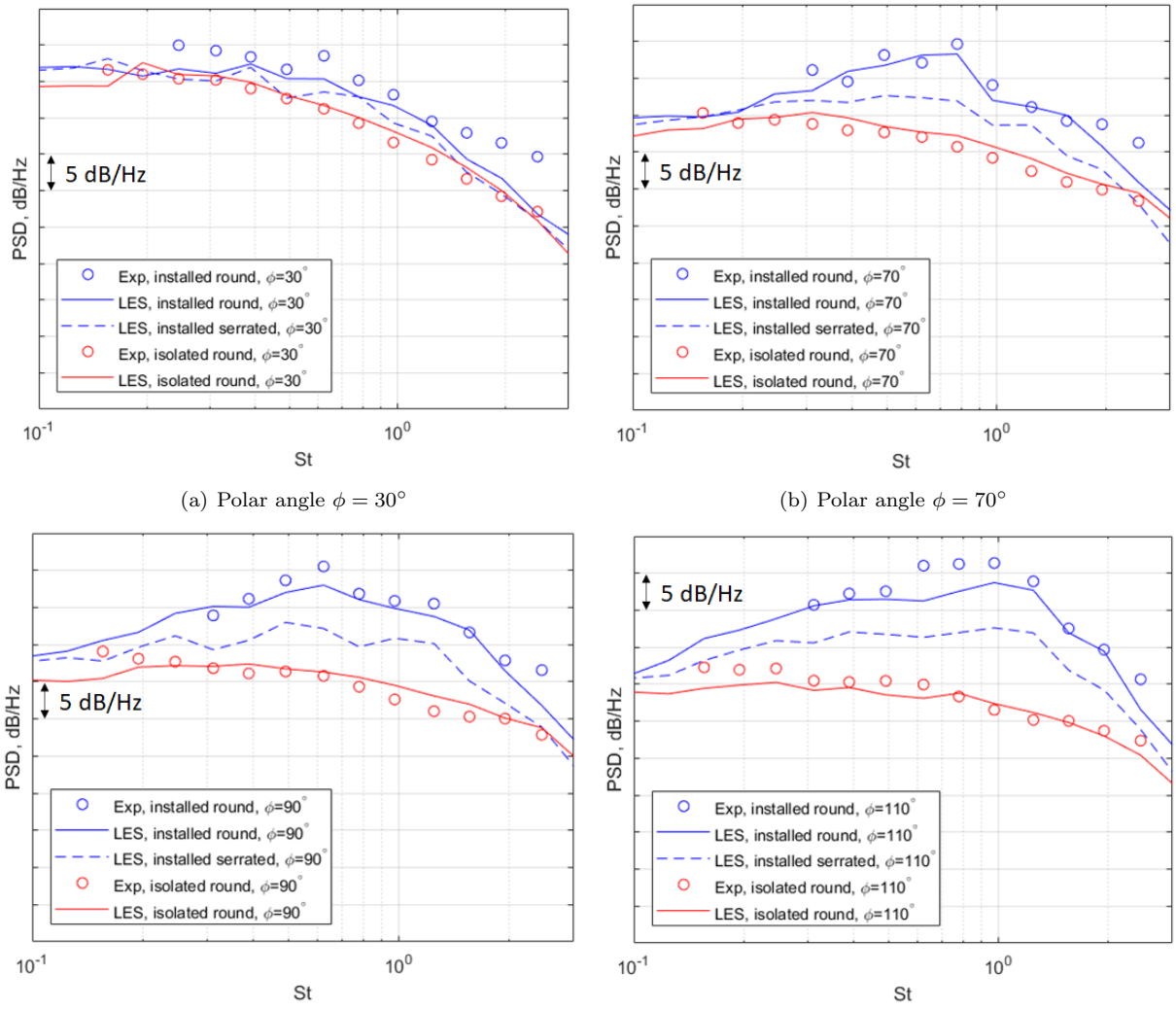

(a) Polar angle $\phi = 30°$

(b) Polar angle $\phi = 70°$

(c) Polar angle $\phi = 90°$

(d) Polar angle $\phi = 110°$

Figure 7. Far-field noise spectra at four polar angles ($\phi = 30°, 70°, 90°$ and $110°$) of the flyover azimuthal position for installed serrated and round nozzle jets

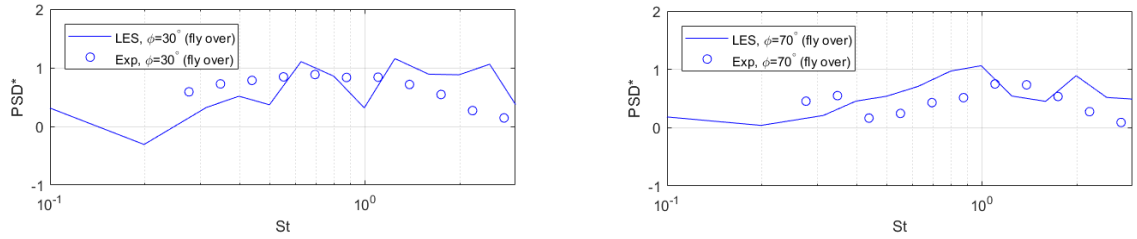

(a) Polar angle $\phi = 30°$

(b) Polar angle $\phi = 70°$

(c) Polar angle $\phi = 90°$

(d) Polar angle $\phi = 120°$

Figure 8. Normalised noise reduction at four polar angles ($\phi = 30°, 70°, 90°$ and $120°$) of the flyover azimuthal position for installed serrated nozzle jets

1. Quadruple sources

Jet mixing noise has been successfully modelled using acoustic analogy.[27,28] Far-field noise is predicted by calculating the convolution of a Green's function with a fourth-order space-time velocity correlation over the source region. The Green's function can be obtained numerically or analytically, depending on the complexity of the propagation problem itself. The fourth-order space-time correlations, characterising mixing noise sources, are informed by LES, written as

$$R_{ijkl}(d\mathbf{x}, \tau; \mathbf{x}) = \overline{T_{ij}(\mathbf{x}, t) T_{kl}(\mathbf{x} + d\mathbf{x}, t + \tau)} \tag{1}$$

where $T_{ij} = -(\rho u_i' u_j' - \overline{\rho u_i' u_j'})$ has a zero mean with $\overline{()}$ representing time averaging, and $u_i' = u_i - \tilde{u_i}$ is the velocity fluctuation with respect to the Favre-averaged value $\tilde{u_i} = \overline{\rho u_i}/\overline{\rho}$. $d\mathbf{x}$ and τ are spatial and temporal separations respectively.

Figure 9 shows the fourth-order correlations of axial velocity fluctuations $R_{1111}\big(d\mathbf{x} = (dx, 0, 0), \tau; \mathbf{x}\big)$ over the axial separation dx and time delay τ along a streamline in the centre of the upper bypass nozzle shear layer from nozzle exit up to the end of potential core. The centre of the space-time correlations $R_{1111}(\mathbf{0}, 0; \mathbf{x})$ are plotted on the line of $\tau U/D = 0$ offset by their axial locations x. The correlations peak at the zero spatial and temporal separations and then decay as the separations increase. The extent of the correlated region is defined as the 'eddy' scale. Within the eddy, the chaotic turbulent motions are statistically correlated and contribute to noise generation. The eddy travels at a convective speed U_c, forming a space-time trajectory in the $\tau - dx$ graph by connecting the axial separations of correlation peak dx_{peak} at each time delay τ. The

convective velocity U_c is around 0.65 U_j for both round and serrated nozzle jets before the potential core end. This convective speed is typical of Kelvin-Helmholtz instability waves.

The eddy correlates over a certain distance and time period, which are characterised by integral length and time scales:

$$L^{x_i}_{ijkl}(\mathbf{x}) = \frac{1}{2}\int_{-\infty}^{+\infty} \frac{R_{ijkl}(d\mathbf{x}, 0; \mathbf{x})}{R_{ijkl}(\mathbf{0}, 0; \mathbf{x})} dx_i \tag{2}$$

$$T_{c,ijkl}(\mathbf{x}) = \int_{0}^{+\infty} \frac{R_{ijkl}(d\mathbf{x}_{peak}, \tau; \mathbf{x})}{R_{ijkl}(\mathbf{0}, 0; \mathbf{x})} d\tau \tag{3}$$

The integral scales are calculated from the space-time correlations along the same streamline inside the bypass shear layer and shown in Fig. 10. Both time and length scales increase in the streamwise direction as the shear layer develops. In general, the serrations slightly reduce the source time and length scales as fine-scale turbulence is induced by serrations, which is qualitatively illustrated in Fig. 6. The jet and wing interactions introduce large scale turbulent motions and a spike in length and time scales is present just downstream of the wing TE between $x/D = 2$ and 3. The serrations have reduced the peak by weakening the interactions with wings. The reduced length and time scales of quadrupole sources potentially contribute to the reduction of mixing noise, as they determine the volume size of quadrupole sources integrated with the Green's function for far-field noise prediction in the Goldstein acoustic analogy.[27]

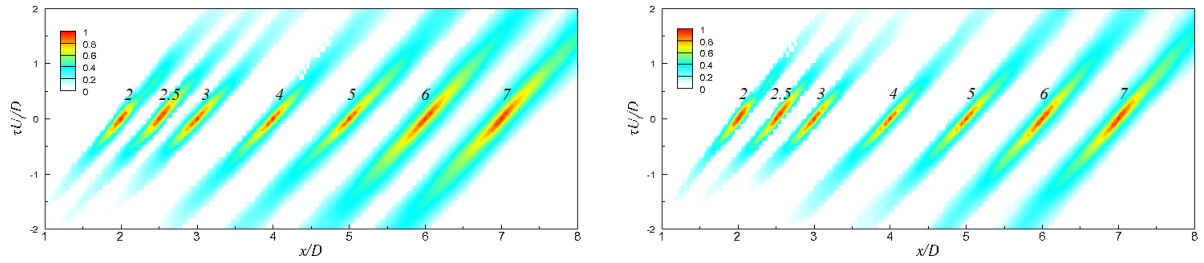

(a) Installed round nozzle jet

(b) Installed serrated nozzle jet

Figure 9. Contours of space-time correlations $R_{1111}\big(d\mathbf{x} = (dx, 0, 0), \tau; \mathbf{x}\big)$ normalised by $R_{1111}(\mathbf{0}, 0; \mathbf{x})$ along the upper bypass nozzle shear layers at the axial locations of $x/D = 1.5, 2, 2.5, 3, 4, 5, 6$ and 7, and at the end of potential core of $x/D = 8$ for the installed round and serrated nozzle jets

The amplitudes of the leading quadrupole source, $R_{1111}(\mathbf{0}, 0; \mathbf{x})$, are shown in Fig. 11 for both round and serrated nozzle jets. The jet and wing interaction introduces extra mixing, which increases the quadrupole source downstream of the wing TE. Compared to the round nozzle jet, the serrations are able to reduce the source amplitude from $x/D = 1$ by intoducing rapidly decaying small-scale turbulence. This consequently weakens the jet-wing interaction and reduces the interaction-induced sound source between $x/D = 2$ and 3. All the components of fourth-order space-time velocity correlations are then normalised by the leading

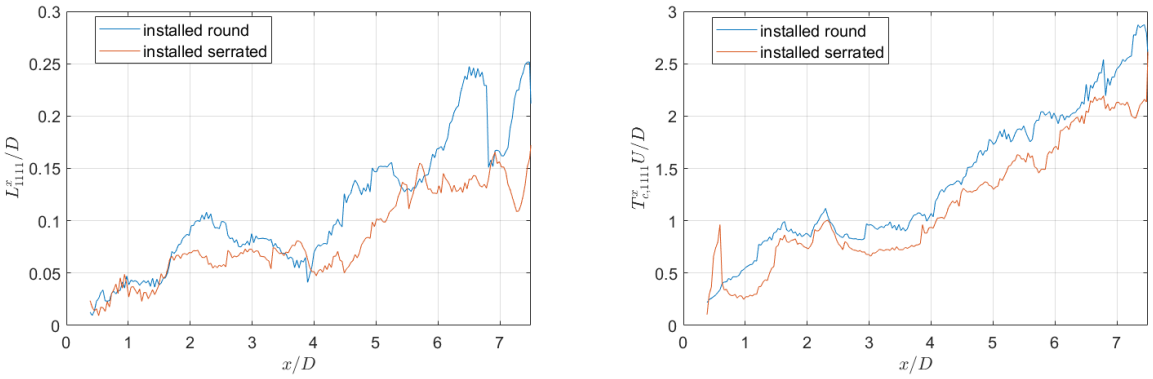

(a) Integral length scale

(b) Integral convective time sacle

Figure 10. Axial integral length and time scales along the shear layers based on the space-timce correlations R_{1111}

component $R_{1111}(\mathbf{0}, 0; \mathbf{x})$. The relative amplitudes of fourth-order velocity correlations are plotted in Fig. 12 at four representative axial positions. Aside of the dominant component R_{1111}, other components, R_{2222}, R_{3333}, R_{1212}, R_{1313}, R_{2323}, R_{1122}, R_{1212}, R_{2212}, and R_{1323}, also contributes to noise production but less significantly. Near the nozzle at $x/D = 1$, the cross velocity correlation components, R_{2222}, R_{3333}, R_{1313}, R_{2323}, are intensified by the serrations, which was found to be proportional to the serration-induced streamwise vorticity.[29] This shows that the serrations increase source anisotropy near the nozzle. Downstream of the wing TE at $x/D = 3$, the magnitudes of the cross velocity correlation components of the serrated nozzle jet are smaller than those of the round jet, which again indicates that the serration has reduced the mixing noise sources caused by jet and wing interactions. Further downstream, at $x/D = 6$ and 10, the serration effects are diminished as the relative correlation amplitudes of serrated nozzle jets return to the same level of round nozzle jet.

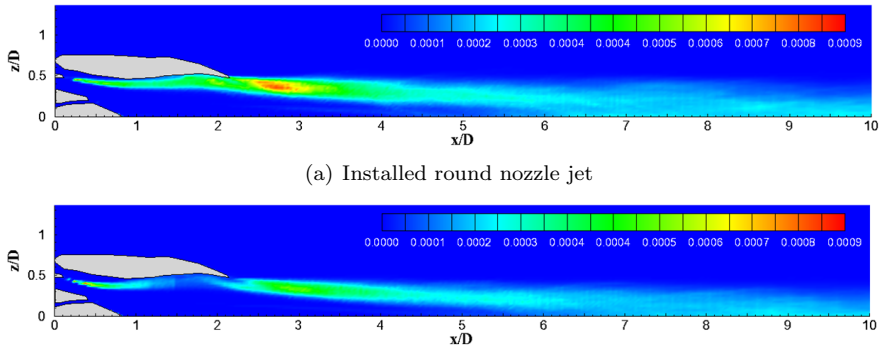

(a) Installed round nozzle jet

(b) Installed serrated nozzle jet

Figure 11. Amplitudes of 4th order axial velocity correlations $R_{1111}(\mathbf{0}, 0; \mathbf{x})/(\rho_j U_j^2)^2$ for the installed round and serrated nozzle jets

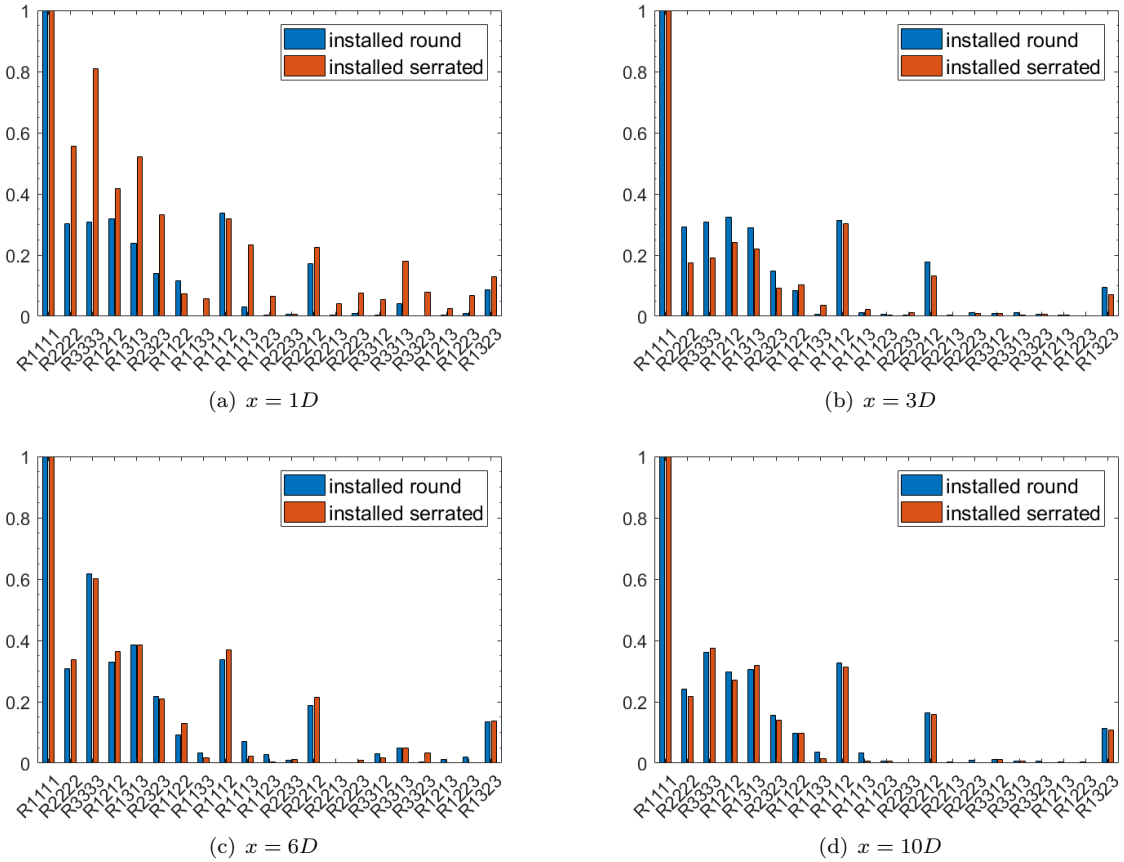

(a) $x = 1D$ (b) $x = 3D$

(c) $x = 6D$ (d) $x = 10D$

Figure 12. Relative amplitudes of 4nd-order space-time correlations $R_{ijkl}(\mathbf{0}, 0; \mathbf{x})/R_{1111}(\mathbf{0}, 0; \mathbf{x})$ at axial location of $x/D = 1, 3, 6$ and 10 in the upper bypass nozzle shear layers

2. Evanescant pressure waves and thier scattering

It has been recently found that the majority of installation noise is produced by the scattering of hydrodynamic instability waves at the wing TE[4] and the far-field noise generated by the TE scattering can be predicted using a transfer function of the spectra of the near-field evanecent instability waves.[3] The instability waves, often referred to as wave packets,[30] are the coherent stuctures of near-field pressure waves generated on top of the turbulent equillibrium state and decays exponentially in the radial direction, hence described as evanescent. These structures can be detected using spectral proper orthogonal decomposition (SPOD) of near-field pressure fluctuations.[31] The SPOD analysis are employed at the $y = 0$ plane for extracting the coherent wave structures and illustrate their scattering near the TE.

The energy spectra of SPOD modes of pressure fluctuations are shown in Fig. 13. The energy contained in each frequency decreases for higher SPOD modes. A large separation of energy is observed between the first and the rest of the modes of the frequency range from $St = 0.1$ to 2. This indicates that a physically dominanting mechanism is present in the flows. The leading SPOD modes are selectively plotted at four representative frequencies in Fig. 14. Coherent structures are clearly present in pressure fluctuations. These coherent structures are considered as hydrodynamic instability waves and can be replicated by linear stability analysis.[30] At a lower frequency, i.e. $St = 0.16$ in Fig. 14(a) and 14(b), the coherent wave structures start downstream of the potential core end. At higher frequencies, i.e. $St = 0.39$, 0.54, and 1.05 in Fig. 14(c) to 14(h), the start of the instability wave moves upstream with a shorter wavelength and the wave scattering at the wing TE becomes more visible. The serrations suppress the instability wave development under the wing, this therefore reduces the scattering of these waves. The pressure spectra at the wing TE in the $y = 0$ plane and the azimuthal decomposition of pressure spectra at the same radius in Fig. 15 also verify the reduction of incident instability wave strength and their scattering by serrations. The near-field pressure spectra in Fig. 15(a) can be considered as the combination of incident pressure waves and scattered waves. The pressure power density of the serration nozzle jet has been reduced at the wing TE over the frequency range from $St = 0.1$ to 3, compared with that of the round nozzle jet. Figure 15(b) also shows significant energy decrease at the first three azimuthal modes of near-field pressure fluctuations at the TE. In addition to the diminished interaction-induced quadrupole source, the weakened pressure waves and their scattering will further contribute to the observed reduction of installation noise for the installed serrated jet.

IV. Conclusion

The serrated nozzle jet installed under a three-dimensional wing has been numerically investigated using hybrid LES-RANS and was compared with the results of the baseline round nozzle jet. In the near field, the jet and wing interaction deflects and squashes the jet plume, manifested in the increase of turbulent kinetic

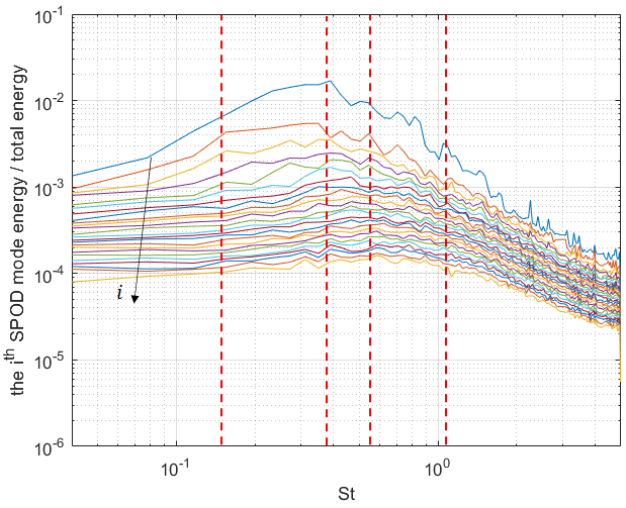

Figure 13. Energy spectra of the first 24 SPOD modes

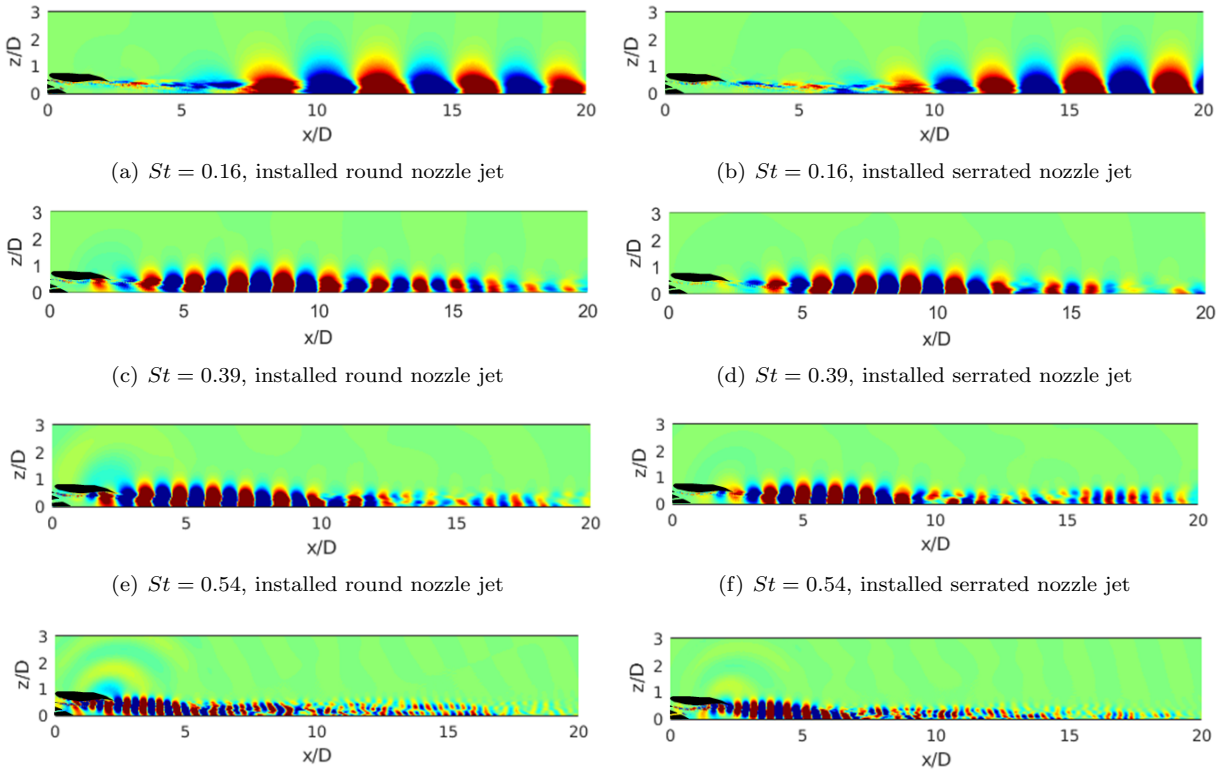

(a) $St = 0.16$, installed round nozzle jet

(b) $St = 0.16$, installed serrated nozzle jet

(c) $St = 0.39$, installed round nozzle jet

(d) $St = 0.39$, installed serrated nozzle jet

(e) $St = 0.54$, installed round nozzle jet

(f) $St = 0.54$, installed serrated nozzle jet

(g) $St = 1.05$, installed round nozzle jet

(h) $St = 1.05$, installed serrated nozzle jet

Figure 14. The first spectral POD mode of pressure fluctuations at $St = 0.16, 0.39$, 0.54 and 1.05 for the installed round and serrated nozzle jets

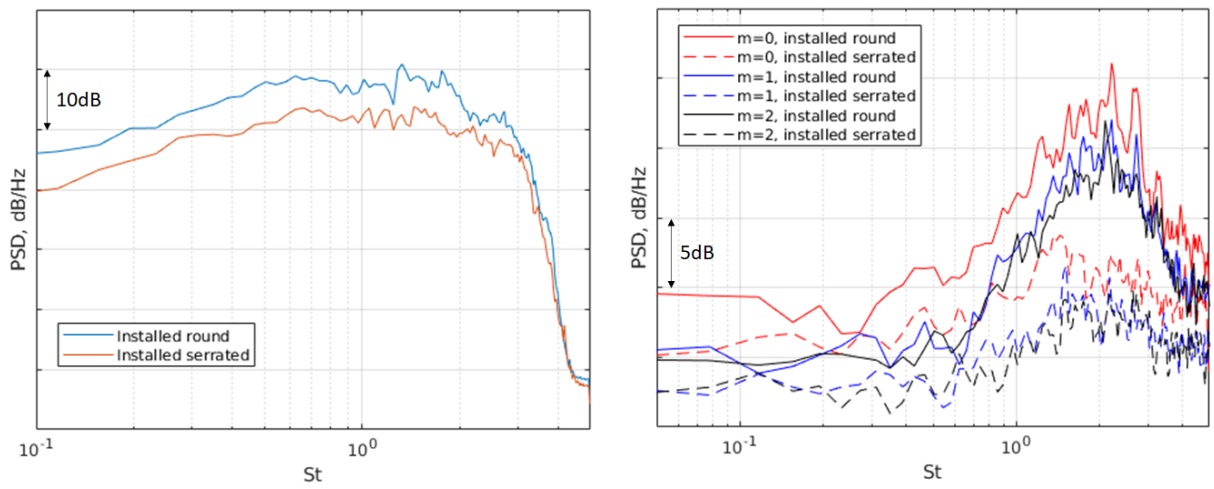

(a) Pressure spectral power density

(b) Azimuthal mode power density

Figure 15. Power spectral density of pressure fluctuations and their azimuthal modes at the wing TE for the installed round and serrated nozzle jets

energy downstream of the wing tailing edge. It is found that the serrations introduce streamwise vortices that break up large-scale azimuthal coherence into small-scale flow structures and enhance the mixing in shear layers. The enhanced mixing dissipates turbulence rapidly before the wing TE and hence reduces the jet and wing interaction. The periodic azimuthal variation introduced by serrations is restricted near the nozzle. It is diminished and gradually returns to that of the round nozzle jet downstream of the wing. In the far field, the noise prediction achieves a satisfactory agreement with the measurements. Installation noise is present in the frequency range from $St = 0.2$ to $St = 2$, and it is more pronounced at the upstream polar angles. The serrations are able to maximally reduce the installed noise by around $5dB$ at the peak frequency. As the grid resolution numerically cuts off the high-frequency spectra, the noise penalty of serrations has not been predicted at high frequencies.

The noise reduction mechanisms are investigated by looking into quadrupole sources and evanescent pressure wave scatterings. Since the serrations have weakened the jet and wing interaction, they decrease the amplitudes of interaction-induced quadrupole sources downstream of the wing TE and reduce the time and length scale growth of the sources. The SPOD results show that the serrations are also able to suppress the pressure waves growth under the wing and lead to a reduction of wave scattering at the TE. Therefore, the serrations reduce installation noise from the sources of both quadrupoles and TE scattering. In the future, the contribution of the two sources to the far-field noise reduction will be further quantified based on the semi-analytical model proposed by Lyu and Dowling[3] and used for optimising serrations for maximum noise reduction of installed jets.

Acknowledgments

The research was conducted under the EU-funded project "JERONIMO" (ACP2-GA-2012-314692-JERONIMO) and the discussions with Dr. Peer Boehning at Rolls-Royce are greatly appreciated. The computational time was provided by the UK Turbulence Consortium under EPSRC grant EP/L000261/1 on the UK national supercomputer ARCHER, the Cambridge Service for Data Driven Discovery (CSD3) under EPSRC Tier-2 and the DECI resource Sisu based in Finland with support from the PRACE aisbl under the project InJet.

References

[1]Lighthill, M. J., *On sound generated aerodynamically II. General theory*,Proceedings of the Royal Society of London. Series A. Mathematical and Physical Sciences, 1952, 211: 564-587.

[2]Williams, J., and Hall, L., *Aerodynamic sound generation by turbulent flow in the vicinity of a scattering half plane*,Journal of Fluid Mechanics, 1970, 40(4): 657-670.

[3]Lyu, B., Dowling, A., and Naqavi, I., *Prediction of installed jet noise*,Journal of Fluid Mechanics, 2017, 811: 234-268.

[4]Piantanida, S., Jaunet, V., Huber, J., Wolf, W. R., Jordan, P., and Cavalieri, A. V. G., *Scattering of turbulent-jet wavepackets by a swept trailing edge*, Journal of the Acoustical Society of America, 2016, 140(6): 4350-4359.

[5]Head, R., and Fisher, M., *Jet surface interaction noise - analysis of far-field low frequency augmentations of jet noise due to the presence of a solid shield*, 1976, AIAA 1976-502.

[6]Brown, C. A., *Jet-surface interaction test: far-field noise results*, Journal of Engineering for Gas Turbines and Power, 2013, 135(7): 071201.

[7]Advisory Council for Aeronautics Research in Europe, *Aeronautics and air transport: Beyond vision 2020 (towards 2050)*, Studies and reports of European Commission, European Research Aeronautics and Air Transport, 2010.

[8]Alkislar, M., Krothapalli, A., and Bulter, G., *The effect of streamwise vortices on the aeroacoustics of a Mach 0.9 jet*, Journal of Fluid Mechanics, 2007, 678: 139-169.

[9]Zaman, K. B. M. Q., Bridges, J. E., and Huff, D. L., *Evolution from tabs to chevron technology - a review*, International Journal of Aeroacoustics, 2011, 10(56): 685709.

[10]Mengle, V. G., Elkoby, R., and Brusniak, L., *Reducing propulsion airframe aeroacoustic interactions with uniquely tailored chevrons: 2. Installed nozzle*, 2007, AIAA 2007-2434.

[11]DeBonis, J. R., *Progress toward large-eddy simulation for prediction of realistic nozzle systems*, Journal of Propulsion and Power , 2007, 23(5): 971980.

[12]Bodony, D. J. and Lele, S. K., *Current status of jet moise predictions using large-eddy simulation*, AIAA Journal , 2008, 46(4): 364380.

[13]Piomelli, U., *Wall-layer models for large-eddy simulations*, Progress in Aerospace Sciences, 2008, 44(6): 437446.

[14]Spalart, P. R., *Detached-eddy simulation*, Annual Review of Fluid Mechanics, 2009, 41(1): 181202.

[15]Wang, Z.-N., Proenca, A., Lawrence, J., Tucker, P. G., and Self, R., *Large-Eddy-Simulation prediction of an installed jet flow and noise with experimental validation*, AIAA Journal, 2020, 58(6): 2494-2503.

[16]Tyacke, J. C., Wang, Z.-N., and Tucker, P. G., *LESRANS of installed ultra-high-bypass-ratio coaxial jet aeroacoustics with flight stream*, AIAA Journal, 2019, 57(3): 1215-1236.

[17]Mockett, C., Fuchs, M., Knacke T., Kramer, F., Michel, U., Steger, M. and Thiele, F., *Industrial prediction of jet-flap*

interaction noise with advanced hybrid RANS-LES methods.,Notes on Numerical Fluid Mechanics and Multidisciplinary Design, 2020, 143: 297-308.

[18]Xia, H. and Tucker, P. G., *Numerical simulation of single-stream jets from a serrated nozzle*, Flow, Turbulence and Combustion, 2012, 88(1): 3-18.

[19]Wang, Z.-N. and Tucker, P. G., and Tucker, P. G., *Large eddy simulation of serration effects on an ultra-high-bypass-ratio engine exhaust jet*, Comptes Rendus Mcanique, 2018, 346(10): 964-977.

[20]Jameson, A., *Formulation of kinetic energy preserving conservative schemes for gas dynamics and direct numerical simulation of one-dimensional viscous compressible flow in a shock tube using entropy and kinetic energy preserving schemes*, Journal of Scientific Computing, 2008, 34: 188-208.

[21]Tyacke, J., Naqavi, I., Wang, Z.-N., Tucker, P., and Boehning, P., *Prediction Large Eddy Simulation for jet aeroacoustics - Current approach and industrial application*, Journal of Turobmachinery, 2017, 139: 081003-1.

[22]Spalart, P. R., and Allmaras, S. R., *A one-equation turbulence model for aerodynamic flows*, La Recherche Aerospatiale, 1994, 1: 5-21.

[23]Smagorinsky, J., *General circulation experiments with the primitive equations. I. the basic experiment*, Monthly weather review, 1963, 91(3): 99-164.

[24]Liu, Y., Tucker, P. G., and Kerr, R. M., *Linear and nonlinear model large-eddy simulations of a plane jet*, Computers and Fluids, 2008, 37(4): 439-449.

[25]Najafi-Yazdi, A., Bres, G. A., and Mongeau, L., *An acoustic analogy formulation for moving sources in uniformly moving media*, Proceedings of the Royal Society of London. Series A. Mathematical and Physical Sciences, 2010, 467(2125): 1-22.

[26]Davy, R., Mortain, F., Huet, M., and Garrec, T. L., *Installed jet noise source analysis by microphone array processing*, 2019, AIAA 2019-2654.

[27]Goldstein, M. E, *A generalized acoustic analogy*, Journal of Fluid Mechanics, 2003, 488: 315-333.

[28]Karabasov, S. A., Afsar, M. Z., Hynes, T. P., Dowling, A. P., McMullan, W. A., Pokora, C. D., Page, G. J., and McGuirk, J. J., *Jet noise: acoustic analogy informed by large eddy simulation*, AIAA Journal, 2010, 48(7): 1312-1325.

[29]Depuru Mohan, N. K., and Dowling, A. P., *Jet-Noise-Prediction Model for Chevrons and Microjets*, AIAA Journal, 2017, 54(12): 3928-3940.

[30]Jordan, P., and Colonius, T., *Wave packets and turbulent jet noise*, Annual Review of Fluid Mechanics, 2013, 45(1): 173-195.

[31]Schmidt, O., Towne, A., Rigas, G., Colonius, T., and Bres, G., *Spectral analysis of jet turbulence*, Journal of Fluid Mechanics, 2018, 855: 953-982.